Bulletin of the Seismological Society of America, Vol. 98, No. 6, pp. 3033–3045, December 2008, doi: 10.1785/0120080082

Short Note

Seasonal Anisotropy in Short-Period Seismic Noise Recorded in South Asia

by Keith D. Koper and Benjamin de Foy

Abstract We present an analysis of seismic noise recorded during 1995–2004 by a medium-aperture, short-period seismic array located in Chiang Mai, Thailand (CMAR). We calculated frequency-wavenumber spectra for nearly 1000 randomly selected time windows, each with a length of 160 sec. At frequencies above about 1.4 Hz the noise is unorganized and the wavenumber spectra are isotropic and diffuse; however, at lower frequencies three robust wavenumber peaks exist. Two of the peaks have phase velocities centered near 4.0 km/sec, consistent with higher-mode Rayleigh waves, while the third peak has much higher apparent velocity (>25 km/sec), consistent with body waves that have interacted with the Earth's core (*PKP*, *PcP*). All three peaks are strongly seasonal with annual power variations of 10–20 dB, and all show excellent correlation in their putative source regions with ocean wave heights derived from TOPEX/POSEIDON satellite tracks. To the best of our knowledge, this is the first time such a high-velocity component of seismic noise has been consistently observed. The presence of this high-velocity peak raises the possibility of using ambient noise to image the Earth's lower mantle and core.

Introduction

Seismometer arrays have been used to study seismic noise at frequencies spanning more than three orders of magnitude, from as low as 0.002 Hz (Rhie and Romanowicz, 2004) to above 2 Hz (Okada, 2003). Arrays are exceptionally useful in noise studies because they provide directional constraints on propagating energy (Rost and Thomas, 2002). Measurements of apparent velocity allow body-wave components of noise to be identified and distinguished from surface wave components (Toksöz and Lacoss, 1968; Haubrich and McCamy, 1969; Lacoss *et al.*, 1969) and allow surface wave dispersion curves to be observed and inverted for geologic models of the subsurface (e.g., Louie, 2001). Measurements of back azimuth allow specific sources of seismic noise to be located (Bungum *et al.*, 1971; Cessaro, 1994; Schulte-Pelkum *et al.*, 2004) and even tracked as a function of time (Gerstoft *et al.*, 2006).

Here we present an analysis of seismic noise recorded over a 10 yr period at a seismic array in Chiang Mai, Thailand. Known as CMAR, the array is a primary station of the International Monitoring System (IMS) and is located at far-regional distances from nuclear test sites in China, India, Pakistan, and North Korea. Part of the motivation for this study is to determine noise characteristics at CMAR that might affect its nuclear monitoring capability. For instance, detection thresholds at CMAR likely depend significantly on the season, direction, and apparent velocity. More generally, the noise characteristics of CMAR are also interesting because they illuminate fundamental dynamic interactions among the oceans, atmosphere, and solid Earth (e.g., Webb, 1998).

Characteristics of CMAR

CMAR consists of 18 vertical-component, short-period, seismometers arranged in a roughly circular geometry (Fig. 1a). The 153 interelement separations range from 1.46 to 10.07 km, and reflect a design goal of detecting teleseismic and far-regional *P* waves at frequencies around 1 Hz. The corresponding array response function (Fig. 1b) is azimuthally symmetric and has side lobes that are small and well separated from the main lobe. The relatively small aperture of CMAR means that relatively small travel-time anomalies at individual elements, caused by 3D earth structure, can lead to biased slowness estimates. Examples of such heterogeneities observed at other arrays include a dipping Moho (Tibuleac and Herrin, 1997), intra-array topography (Bokelmann, 1995), and general variations in geology (Engdahl and Felix, 1971).

Fortunately, such slowness biases have been found to be relatively mild at CMAR (Bondar *et al.*, 1999). In that study, the authors compared observed and predicted slowness vectors at CMAR for a large number of well-located earthquakes

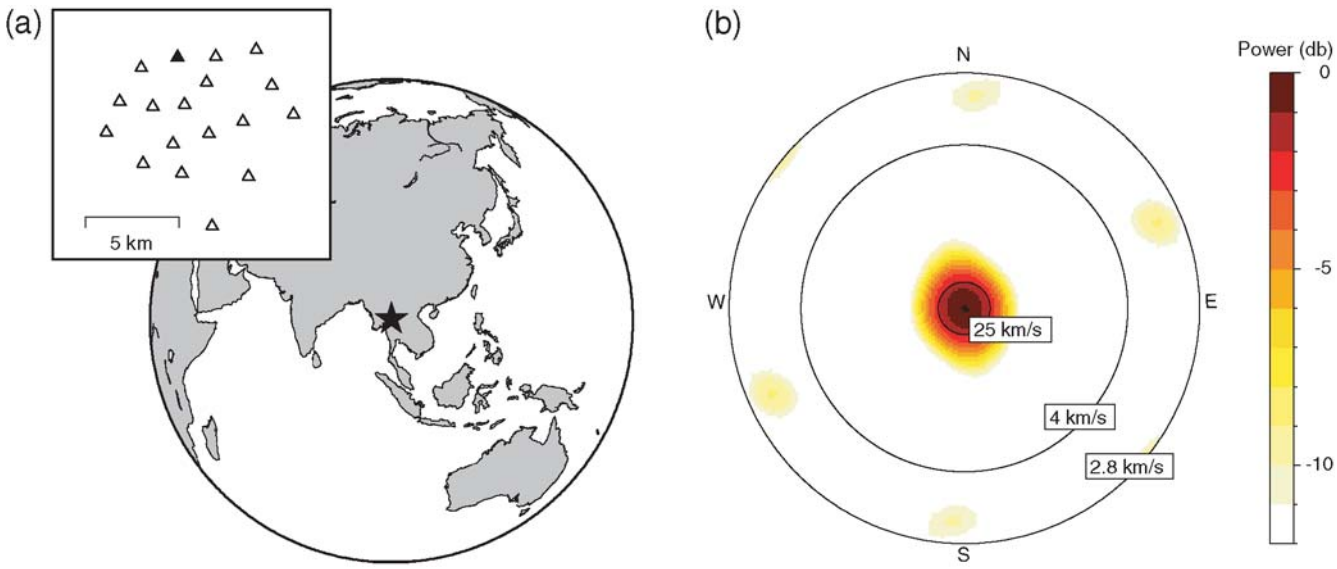

Figure 1. (a) Location and geometry of the Chiang Mai seismic array (CMAR). The dark triangle is the reference point for the array. (b) The array response function for a vertically incident 1 Hz plane wave. Note that the side lobes are distant and weak. At lower frequencies, the side lobes are even farther separated from the main lobe in slowness space.

and found a median ray parameter anomaly of -1.35 ± 0.58 sec/deg and a median back-azimuth anomaly of $7.3° \pm 12.43°$. Most of this bias can be counteracted by applying corrections of -1.622 and 0.208 sec/deg to observations of east–west and north–south slowness, respectively. The bias can be completely eliminated if additional, directionally dependent, corrections are applied (Bondar *et al.*, 1999). Therefore, energy peaks in frequency-wavenumber (*f-k*) spectra observed at CMAR can be confidently backprojected to general geographical regions.

Computing *f-k* Spectra at CMAR

We extracted 955 time windows of seismic noise recorded at CMAR from 1995 through 2004. The 160 sec long windows were chosen to end several tens of seconds in advance of *P* waves from a population of regional distance earthquakes that were analyzed in a related study. The time windows occur in all months, years, and hours of the day and have a quasi-random distribution. All the data were visually inspected, and channels that had glitches or null segments were removed. An average of 15.2 channels per noise window were acceptable.

We used two complementary methods to study the slowness of the CMAR seismic noise. The first is a classic frequency domain method (Capon, 1969) that averages over time and has relatively high resolution in frequency. The second is a time-domain beampacking method (e.g., Schweitzer *et al.*, 2002) that averages over frequency and has relatively high resolution in time. For both methods we assumed that the seismic noise was stationary in time and space over the sample interval. We also ignored elevation differences among the array elements and considered only 2D wavenumber vectors. This is appropriate because CMAR is relatively flat, having a maximum elevation difference of only 0.066 km, compared to a horizontal aperture of 10.1 km (see Bokelmann [1995] for a discussion of topographic effects on slowness inference).

The frequency-domain technique is a high-resolution, direct segment approach (Capon, 1969) described as follows. For each of the 18 channels of CMAR data, we extract 3200 data points and subdivide them into 25 nonoverlapping, adjacent subwindows of 128 samples each. The sampling interval at CMAR is 0.05 sec, so each subwindow is 6.4 sec long and the total window length is 160 sec. For each subwindow and channel the mean is removed, a Bartlett taper is applied, and a fast Fourier transform (FFT) is calculated. For each subwindow, the 18 by 18 spectral matrix is calculated by multiplying the FFT of each channel by the complex conjugate of the FFT of every other channel. These 25 spectral matrix estimates are then linearly averaged to produce a single estimate with reduced variance. Also, by averaging more subwindows (25) than channels (18) the spectral matrix estimate will normally become nonsingular. Finally, the matrix is normalized by dividing each element, S_{jl}, by $\sqrt{S_{jj}S_{ll}}$. This corrects for unequal gain among the seismometers at CMAR.

For a given wavenumber vector, $\mathbf{k} = (k_x, k_y)$, and frequency, f_p, the power spectrum is defined as

$$P(f_p, \mathbf{k}) = \frac{1}{J^2} \sum_{j=1}^{J} \sum_{l=1}^{J} w_l(f_p) w_j^*(f_p) S_{jl}(f_p) e^{2\pi i \mathbf{k}\cdot(\mathbf{x_j}-\mathbf{x_l})}, \quad (1)$$

where $\mathbf{x_j}$ is the position vector of the *j*th seismometer relative to the array reference point and *J* is the number of channels (18). This expression can also be written as a single sum if

the set of all spatial difference vectors, called the coarray, is defined. The element weights, w_j, define a 2D spatial windowing function that is analogous to the Bartlett taper applied in the time domain before the FFT. Here, we use expressions developed for a maximum likelihood filter that passes energy at a given wavenumber in an optimal least-squares sense (Capon, 1969). Discussions of various strategies for choosing these weights are given elsewhere (Burg, 1964; Haubrich, 1968; Ingate *et al.*, 1985; Douglas, 1998).

With the time windows chosen in this work, the frequency interval at which $P(f_p, \mathbf{k})$ is calculated is 0.16 Hz. For a given frequency, we define a wavenumber grid such that the corresponding slowness grid varies from −40 to 40 sec/deg in increments of 0.5 sec/deg and evaluate $P(f_p, \mathbf{k})$ and at each node. The grid is set up in Cartesian coordinates and aligned such that the x component of slowness ($s_x \equiv k_x/f_p$) is east–west and the y component of slowness ($s_y \equiv k_y/f_p$) is north–south. The back azimuth is defined clockwise from north as $\arctan(s_x/s_y)$, and the ray parameter is defined in units of seconds per degree as $\sqrt{s_x^2 + s_y^2}$. We also define the apparent or phase velocity in units of kilometers per second as the inverse of the ray parameter.

The time-domain technique is based on algorithms previously developed for analysis of coda waves and small amplitude body waves (Koper *et al.*, 2004). In this approach we first extract time windows of length 64 sec from each of the 18 channels at CMAR. For each trace we remove the mean, apply a three pole Butterworth band-pass filter, and resample the data from 0.05 to 0.01 sec. The corner frequencies of the filter are either 0.33–0.67, 0.67–1.33, or 1.33–2.67 Hz. A slowness grid with the same dimensions as used previously is constructed, and a phase stack weighted beam (Schimmel and Paulssen, 1997) of order three is formed at each node. The power is defined as the mean-square amplitude of the beam over the 64 sec time window. This approach is more computationally intensive than the frequency-domain approach, which is why we use a shorter time window (64 versus 160 sec). In all cases, the window for the time-domain method is chosen as the first 64 sec of the corresponding 160 sec window.

Example spectra are shown in Figure 2 for a typical time window. Power is plotted in decibels relative to the sample maximum, $10\log_{10}(P/P_{\max})$, and the color scale is chosen such that only energy at least 10% of the maximum is highlighted. Agreement between the techniques is good, especially considering that the time and frequency sensitivities are different. The time-domain technique gives slightly sharper images, probably because it amplifies coherent energy via phase-weighted stacking. In both methods, at higher frequencies the noise power becomes diffuse and unorganized while at lower frequencies there are specific preferred directions. As we discuss later, the preferred noise directions at CMAR are generally stable from one time window to the next, though the absolute amplitudes exhibit strong variability.

Ocean Wave Heights from TOPEX/POSEIDON Data

To help interpret noise peaks observed in *f-k* spectra at CMAR, we used a global model of ocean wave height determined from satellite data. Because ocean waves play a dominant role in generating microseismic noise, it follows that wave heights in oceanic source regions should have a high correlation with time series of the corresponding microseismic energy. On the other hand, oceanic regions with wave heights that show poor or negative correlations with microseismic energy can be eliminated as potential source regions.

Significant wave heights, defined as the mean height of the highest 33% of ocean waves, were obtained from the Ku-band of the TOPEX/POSEIDON satellite altimetry mission (Callahan *et al.*, 1994) via the merged geophysical data record (MGDR) distributed by the National Aeronautics and Space Administration (NASA) Jet Propulsion Laboratory (JPL). The satellite has a 10 day repeat orbit with a maximum orbiting latitude of 66°, and data reported every second are averages of the values obtained from 10 Hz measurements. Using data for which at least six values were used in the average and for which the root mean square error of the six or more values was below 1 m, we calculated average monthly ocean wave heights over 2° by 2° grids for the same 10 yr period (1995–2004) as the seismic noise data. Excluding grids that contained some fraction of land cover and those that were beyond ±60° in latitude and so less robust, this led to 8488 distinct time series of ocean wave height. We also used this procedure to process the satellite data recorded over four customized oceanic regions that were each about four times larger in area than the 2° by 2° grids.

Interpretation of *f-k* Spectra at CMAR

Average Results

Noise power as a function of slowness is shown in Figure 3 as an average over the 955 time windows. Individual spectra were normalized before contributing to the stack; therefore, the relatively few windows that inadvertently contain large, earthquake generated signals do not bias the overall result. At frequencies above about 1.4 Hz, the noise is incoherent and isotropic, and the two methods give dissimilar results. However, at lower frequencies the seismic noise is strongly anisotropic, relative to both back azimuth and apparent velocity, implying that it is organized as propagating plane waves.

At lower frequencies the two methods give similar results, showing three distinct, robust peaks. These peaks are broadened somewhat because each noise source varies within a general geographic region; however, each of the three noise sources is clearly localized as shown by the

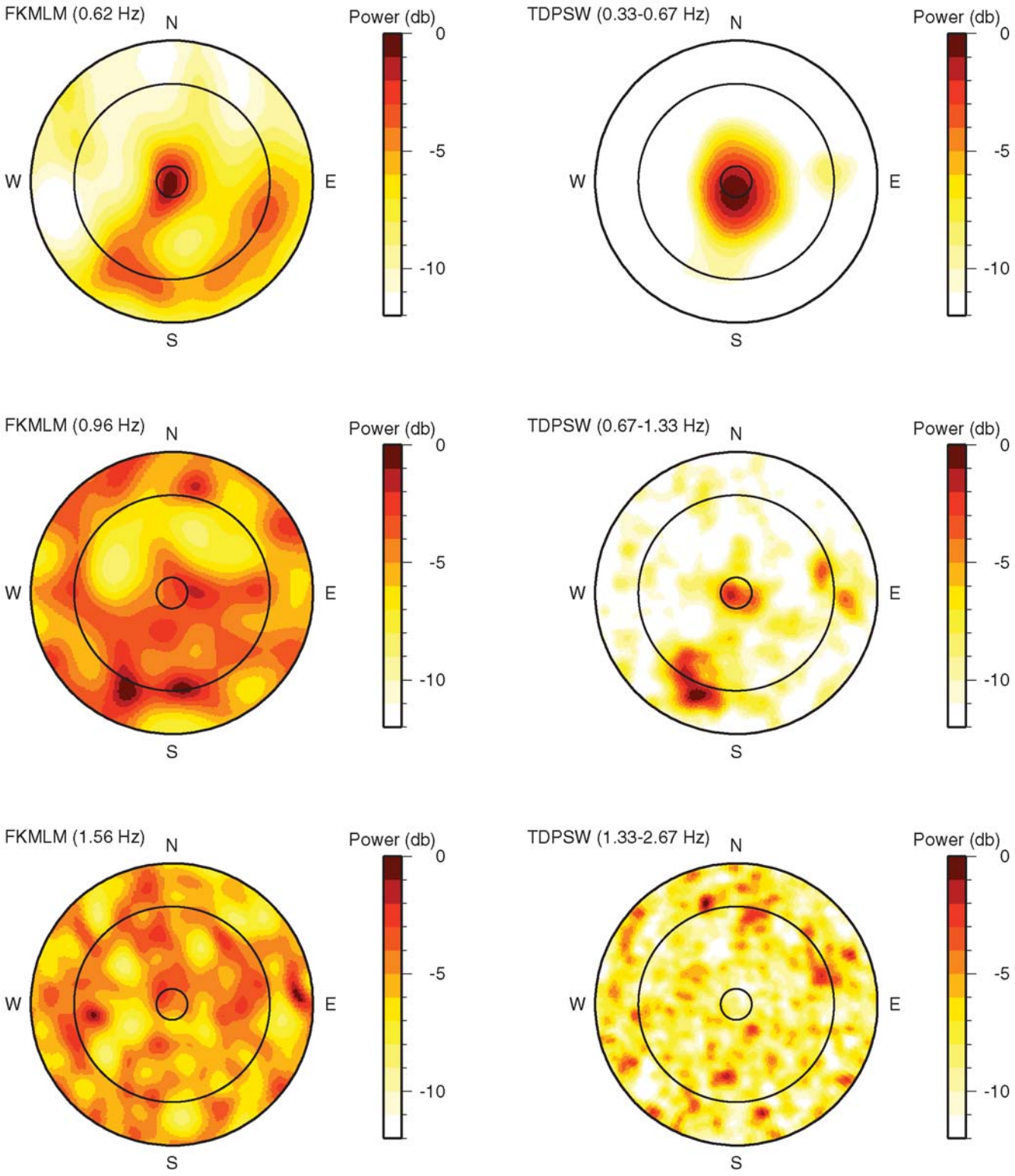

Figure 2. *f-k* spectra for a time window of seismic noise starting at approximately08:30:00 UTC on 26 March 1996. The panels on the left show results from the frequency-domain technique (*f-k* maximum likelihood method [FKMLM]) for a 160 sec time window, and the panels on the right show results from the time-domain technique (time-domain phase stack weighting [TDPSW]) for a 64 sec subwindow. Frequency increases from top to bottom in both cases. The inner ring indicates a ray parameter of 4.4 sec/deg (phase velocity of about 25 km/sec), the middle ring indicates a ray parameter of 27.8 sec/deg (phase velocity of 4 km/sec), and the outermost ring indicates a ray parameter of 40.0 sec/deg (phase velocity of about 2.8 km/sec). Therefore, energy arriving within the inner ring possesses a ray parameter smaller than P_{diff} and so has likely interacted with the Earth's core. Energy arriving between the two outer rings is consistent with higher-mode Rayleigh waves and is typical of short-period noise recorded at arrays.

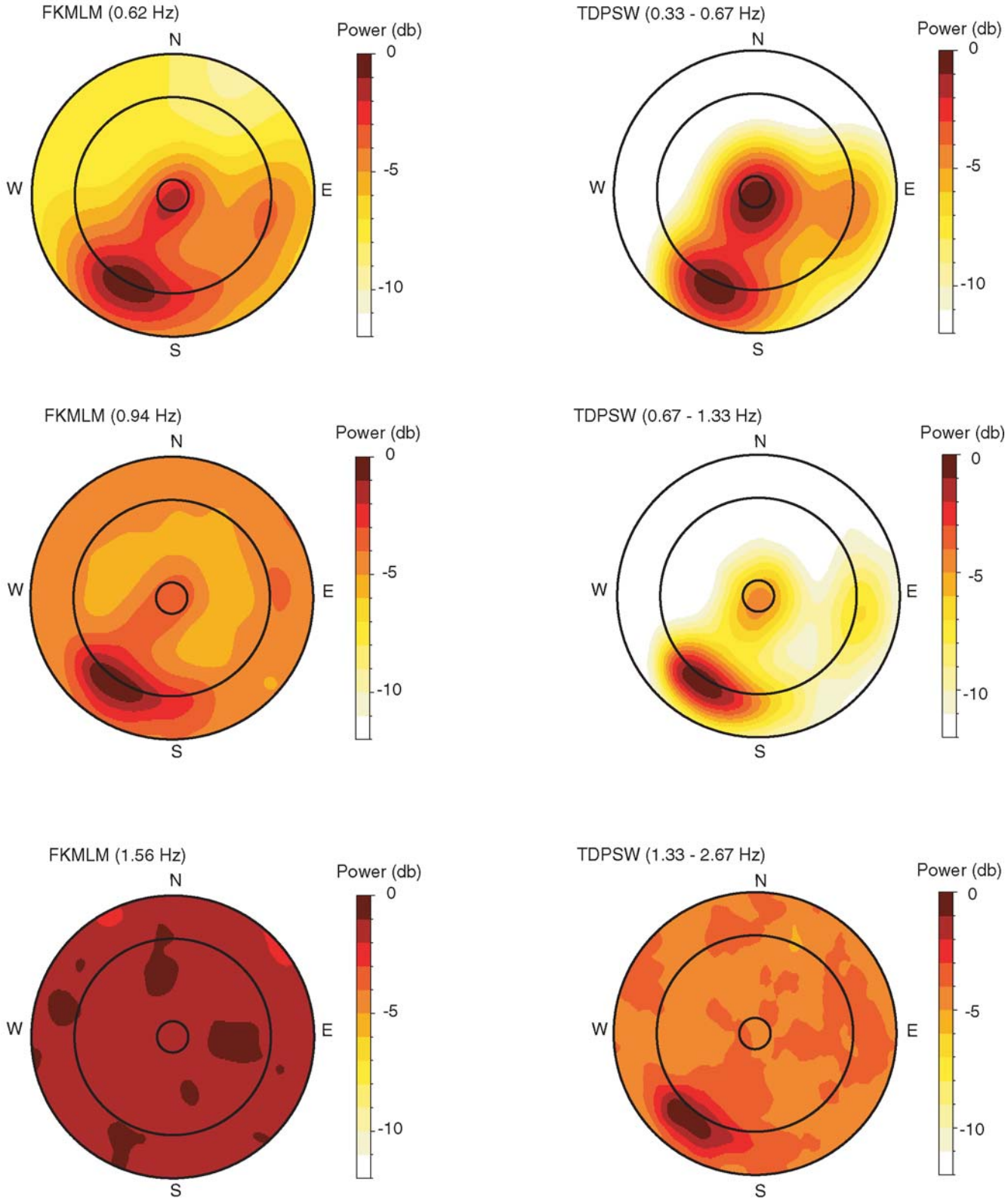

Figure 3. Stacked *f-k* spectra for the 955 time windows. Subpanels are the same as described in Figure 2.

sharpness of the corresponding histograms of peak noise power (Fig. 4). In that figure we also show the effect of the slowness corrections of Bondar *et al.* (1999). We implemented the default correction to all observations and further applied the directionally dependent corrections to those observations falling within the appropriate bins in slowness space. As expected, the corrections have little effect on the overall pattern of noise peaks.

It is important to emphasize that none of the three noise peaks shown in Figures 3 and 4 are side lobes of one another.

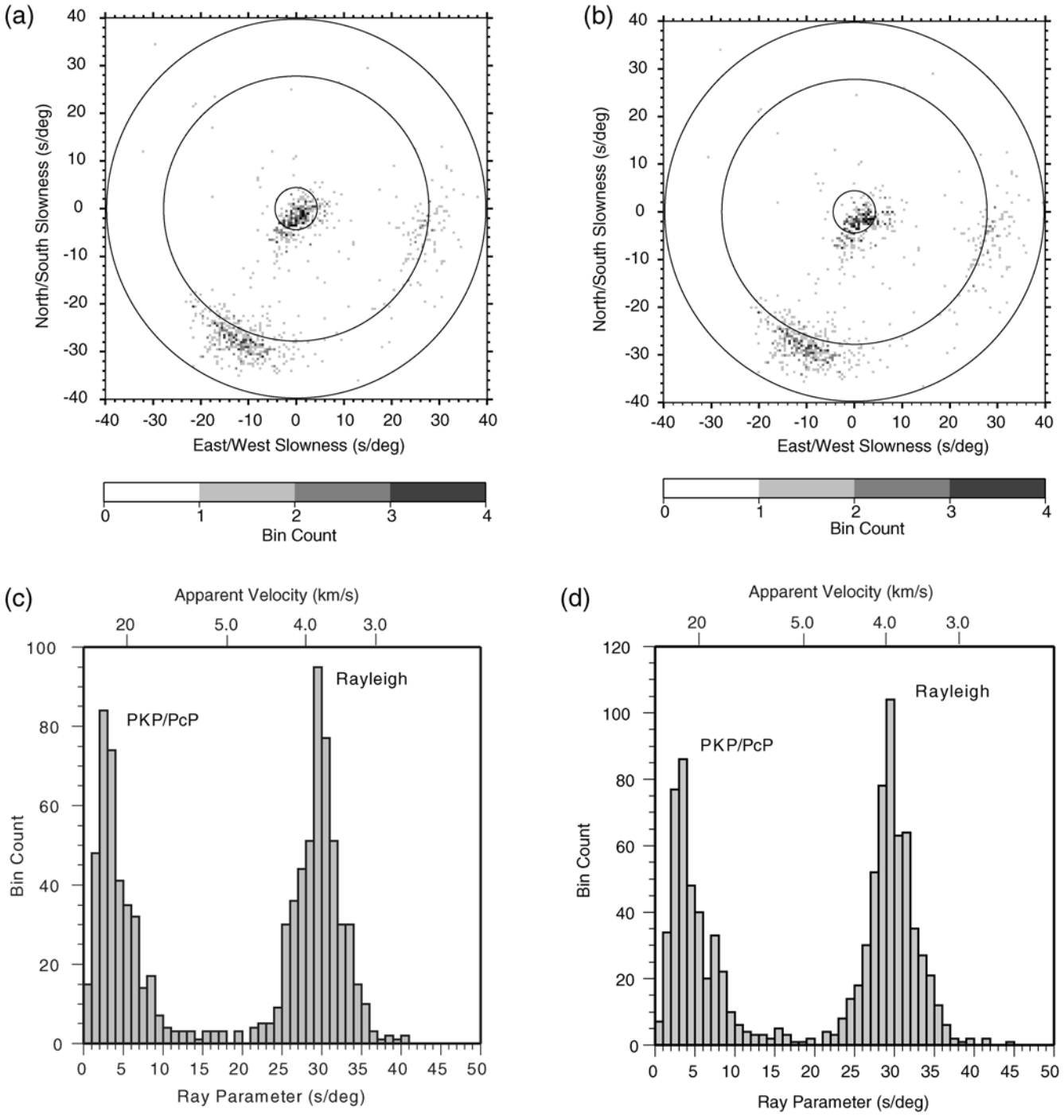

Figure 4. Histograms of peak noise power for the 955 time windows. The global maxima were selected from the time-domain algorithm applied in the 0.33–0.67 Hz band. We show the full 2D histogram in 0.5 by 0.5 sec/deg bins with circles drawn at apparent velocities of 25, 4, and 2.8 km/sec for the (a) raw and (b) corrected slownesses. The corresponding ray parameter histograms in bins of 1 sec/deg are shown in panels (c) raw and (d) corrected.

This is evident by examining the CMAR array transfer function, shown in Figure 1b at 1 Hz, and realizing that at lower frequencies the side lobes are even more distant in slowness space. Furthermore, both of the spectral estimation techniques we used reduce the amplitude of spurious peaks, with the frequency-domain technique in particular essentially deconvolving the array transfer function from the observed spectra (Capon, 1969).

Rayleigh Noise from the East

The weakest of the three noise peaks shown in Figure 3 has apparent velocities centered near 4.0 km/sec (indicative of higher-mode Rayleigh waves) and arrives from the east at back azimuths of 80°–120°. The seismically estimated source area for this Rayleigh energy is shown in Figure 5 as a wedge-shaped region extending eastward from CMAR across Vietnam into the South China Sea. We arbitrarily

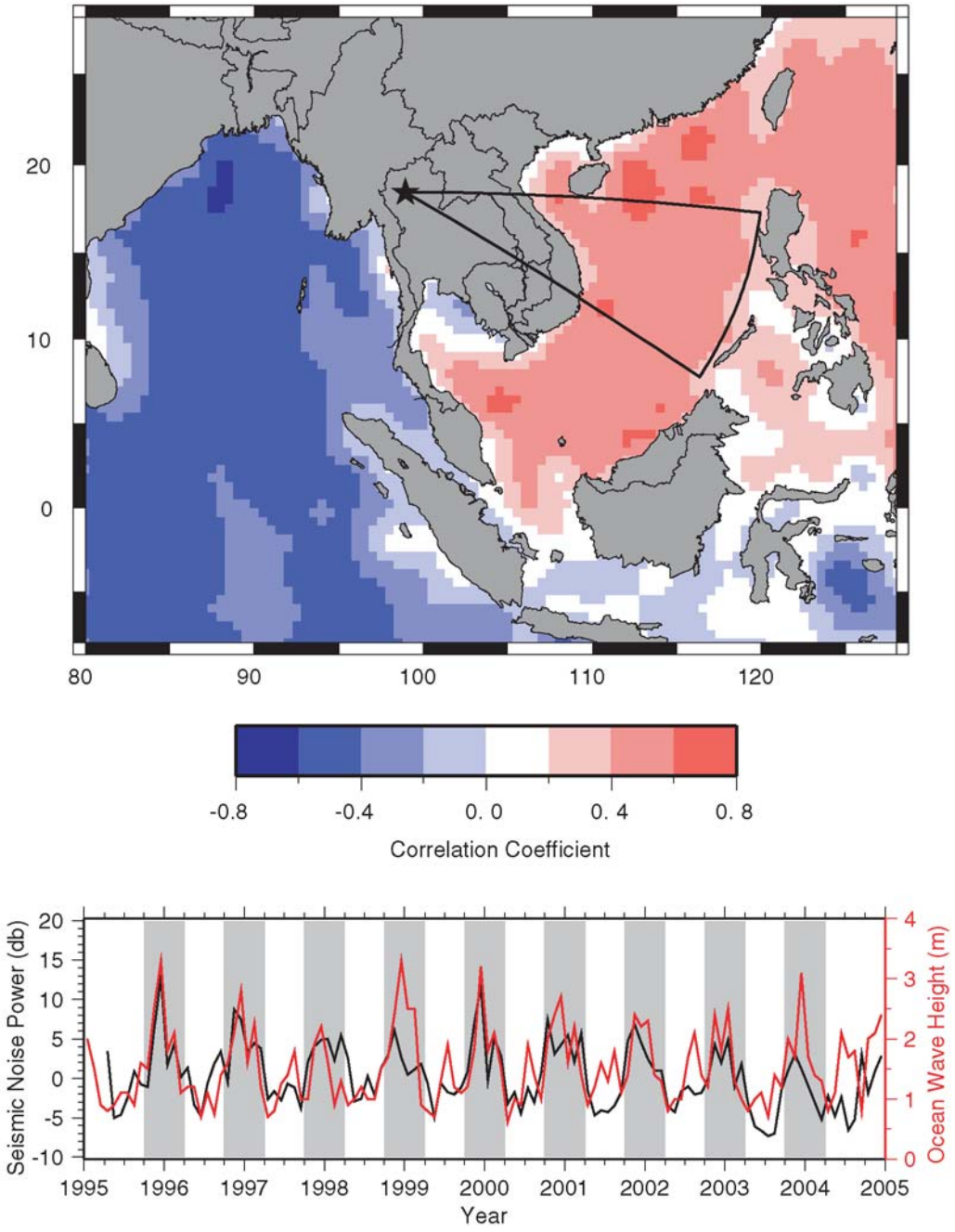

Figure 5. Correlation of the Pacific Ocean Rayleigh-wave microseismic energy with ocean wave heights. In the top panel the seismically constrained source area is shown by the wedge shape, and the color indicates the correlation coefficient between the seismic noise and the significant ocean wave heights. The time dependence of the seismic noise is shown by the black curve in the bottom panel, and the red curve represents significant wave height for a domain of 11°–15° N and 111°–115° E

bounded the source region at a distance of 20° because of the high attenuation of short-period Rayleigh waves.

Surface waves are commonly observed in microseismic noise, and excitation of the double frequency mode (periods of 6–10 sec) can be explained by counterpropagating ocean waves that interfere in a nonlinear manner (Longuet-Higgins, 1950). Our observations fall on the short-period side of this peak but can nevertheless be explained, for instance, by the interference of ocean waves incident on and reflected by the Vietnamese coastline. Little seismic noise is observed from the northern Vietnamese coast in the Gulf of Tonkin, which is presumably shielded from the Pacific Ocean by the island of Hainan. Likewise, the main island of Malaysia probably acts as a buffer to the south.

We examined the time dependence of this seismic noise source using the following procedure. For each of the 955 time windows we selected the maximum power in the region of slowness space bounded by 3.0–6.0 km/sec in apparent velocity and 70°–125° in back azimuth, as measured on the slowness grid calculated with the time-domain method in the 0.5 Hz frequency band. We found the median value, and then converted each observation into decibels relative to this median. We next removed nearly 20 samples that were more than 20 dB above the median, eliminating the effect of earthquake energy, and then averaged the remaining samples into monthly bins. The resulting curve is shown in black in the bottom panel of Figure 5. It is strongly seasonal with peaks in local winter and troughs in local summer, and it has a dynamic range of 10–15 dB.

The time dependence of the seismic noise is well-correlated with variations in significant wave height for many nearby geographical regions. We demonstrate this by calculating the correlation coefficient between the seismic noise time series (Figure 5) and the significant wave height time series (not shown) for each 2° by 2° grid of ocean surface in the region. These coefficients are smoothed and plotted as the background color in the top panel of Figure 5. Values directly adjacent to coastlines are biased a little by the smoothing algorithm, but it is clear that wave heights across the entire South China Sea are highly correlated with the seismic noise. The 99% level of significance is given by a coefficient of 0.22; therefore, the waves at any region shown in a shade of red have a statistically significant correlation with the microseismic noise. As a direct comparison to the seismic noise, we show the time series of significant wave height averaged over the region of 11°–15° N and 111°–115° E as the red curve in the bottom panel of Figure 5.

Rayleigh Noise from the Southwest

The largest noise peak shown in Figure 3 arrives from the southwest at back azimuths of 180°–225° and also has phase velocities centered near 4.0 km/sec. The inferred source region is indicated by the wedge shape in Figure 6. Geographically it corresponds to the Burmese coastline from the border with Thailand in the south to the peninsular Pagoda Point in the north. At slightly larger back azimuths of 230°–280°, relatively little seismic noise is generated even though the nearby coastlines of western Burma, Bangladesh, and northeastern India lie in this direction. Likewise, there is relatively little seismic noise generated at back azimuths of 135°–180°, corresponding to coastlines of the Malay Peninsula and the Gulf of Thailand. These two seismically quiet regions are likely shielded from northeasterly travelling storms by Sri Lanka and Indonesia, respectively, while the narrow region in between is subjected directly to the prevailing currents and swell of the larger Indian Ocean.

The time dependence of the Indian Ocean seismic noise was calculated in a similar manner as was done for the Pacific Ocean noise, including the same normalization value, but with the relevant region of slowness space defined by apparent velocities of 3.0–6.0 km/sec and back azimuths of 180°–260°. The resulting curve is shown in black in the bottom panel of Figure 6. The median of these values is 4.1 times larger than the median of the Pacific Ocean values. Two factors are likely responsible for the increased power. First, there is larger fetch across the Indian Ocean than the South China Sea, so the excitation of the Rayleigh energy on the southern Burmese coast is probably stronger than the excitation along the Vietnam coast. Second, the seismic propagation path from the coastline to CMAR is shorter for the Indian Ocean noise source and so lower attenuation of the short-period Rayleigh energy is expected.

Like the Pacific Ocean noise, the Indian Ocean noise is strongly seasonal with a dynamic range of 10–15 dB; however, the seasonal variation is opposite, with peaks in local summer and troughs in local winter. This phenomenon is well explained, though, by the seasonal variation of wave heights in the Indian Ocean, as shown by the high correlation coefficients in Figure 6. These waves peak in the northern summer (southern winter) because the Indian Ocean as a whole has southern hemisphere dynamics. Thus, the seasonal anticorrelation of wave heights in the Pacific and Indian Oceans is mimicked by the seasonal anticorrelation of seismic noise from these regions.

Teleseismic Body-Wave Noise

The third noise peak shown in Figure 3 occurs near the center of the diagram, indicating energy that is almost vertically incident on the array. Ray parameters for this peak are clustered between 0 and 5 sec/deg, with a mean near 2.5 sec/deg for the uncorrected data (Fig. 4c) and a mean near 3.5 sec/deg for the corrected data (Fig. 4d). Owing to the near-vertical incidence, the back azimuths are poorly resolved, though there is a trend toward the southeast. The ray parameter for P waves that turn just above the core–mantle boundary (equivalently P_{diff}) is about 4.4 sec/deg, so the fact that we observe smaller values implies that the noise is composed of P waves that have interacted with the Earth's core.

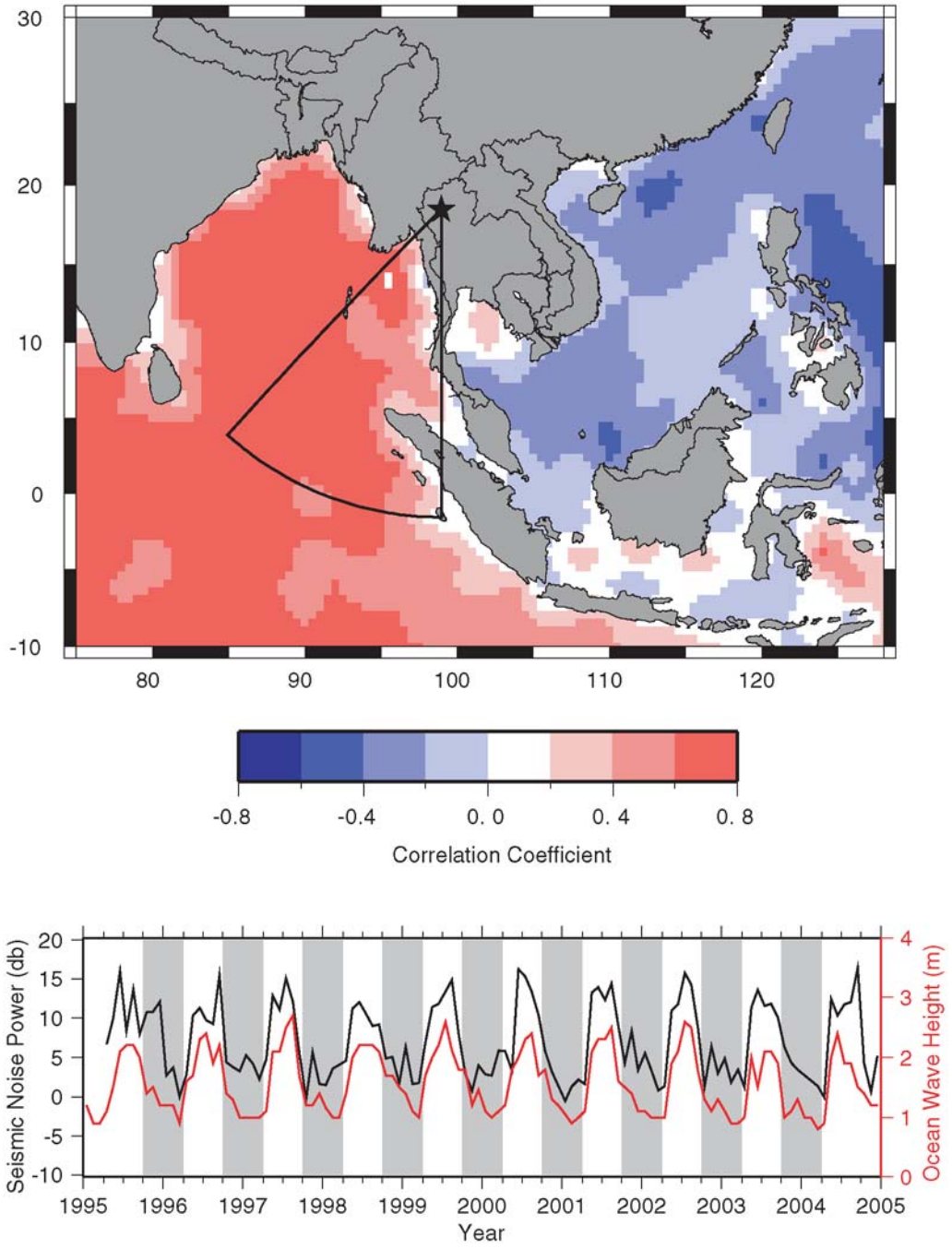

Figure 6. Correlation of the Indian Ocean Rayleigh-wave microseismic energy with ocean wave heights. In the top panel the seismically constrained source area is shown by the wedge shape, and the color indicates the correlation coefficient between the seismic noise and the significant ocean wave heights. The time dependence of the seismic noise is shown by the black curve in the bottom panel, and the red curve represents significant wave height for a domain of 8°–12° N and 91°–95° E.

We first consider the possibility that the waves have been transmitted through the core as *PKP* waves and assume that the noise source occurs at a distance of 140°–145° from CMAR, as shown in Figure 7. This range brackets the $PKP - B$ caustic, a distance at which energy is geometrically focused to a maximum by the velocity structure in the Earth's core. We note that previous observations of *P* waves in microseismic noise have generally occurred at ray parameters consistent with a distance of 20° (Haubrich and McCamy, 1969; Gerstoft *et al.*, 2006), a range in which body-wave energy is also geometrically focused, in this case by high-velocity gradients in the mantle transition zone.

The time dependence of the *P*-wave noise is shown by the black line in the bottom of Figure 7. It was calculated, in the manner described earlier, from the region of slowness space with velocity greater than 20 km/sec (with a ray pa-

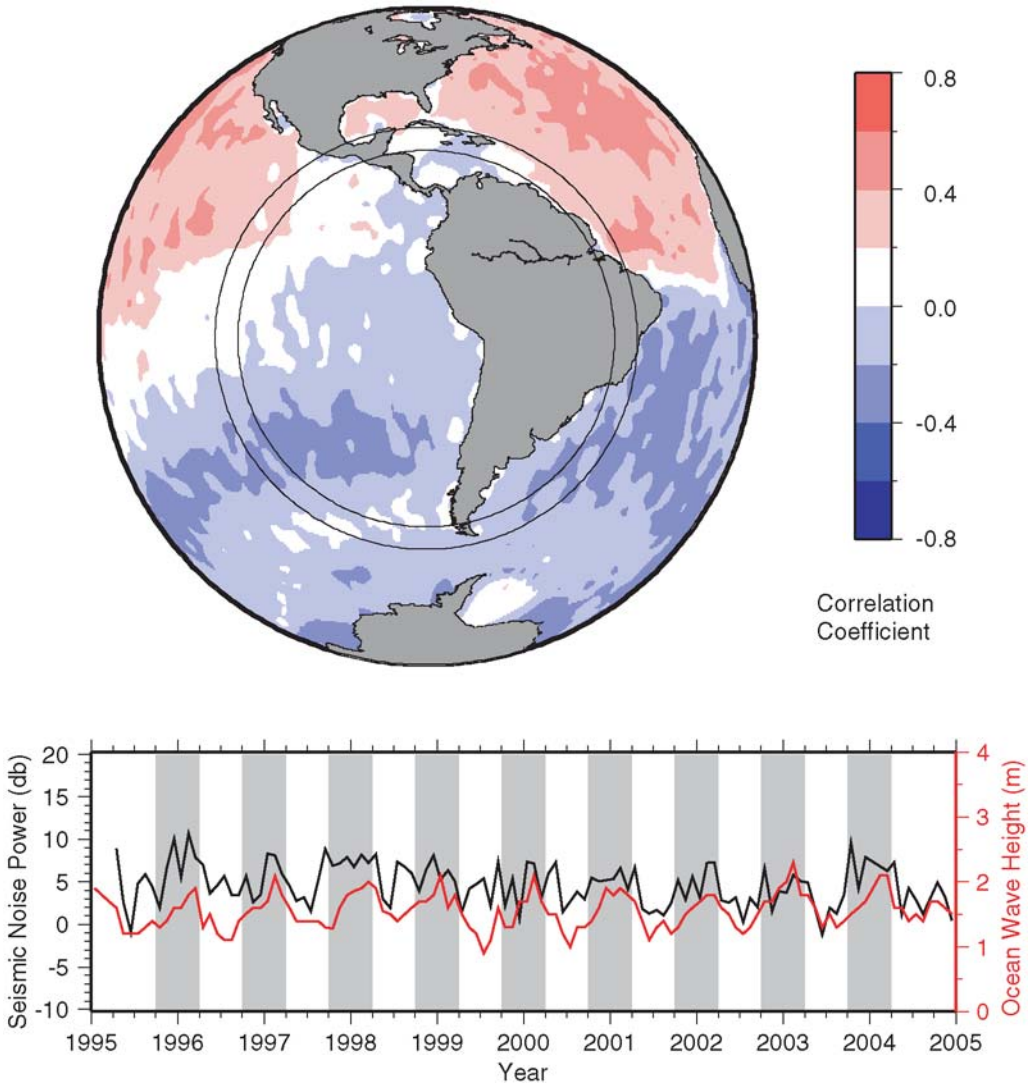

Figure 7. Correlation of the high-velocity microseismic energy with ocean wave heights, assuming a *PKP* source. In the top panel the seismically constrained source area is shown by the annulus, and the color indicates the correlation coefficient between the seismic noise and the significant ocean wave heights. The time dependence of the seismic noise is shown by the black curve in the bottom panel, and the red curve represents significant wave height for a domain near the north coast of Brazil defined as 2° S–3° N and 50°–45° W.

rameter less than 5.5 sec/deg), and it has a median that is 3.1 times larger than the median of the Pacific Ocean Rayleigh noise. There is a clear seasonality to the seismic noise, with peaks in the northern winter and troughs in northern summer, though the dynamic range is only 5–10 dB. The correlation of the seismic noise with ocean wave heights across the hypothetical *PKP* source region is also shown in Figure 7. While it is tempting to suggest that the strong waves near the southern tip of South America create *PKP* noise at CMAR, no significant correlation was found with the seismic observations. The only portion of the seismic source annulus that gives high correlation is the patch along the northern coast of Brazil near the Amazon delta. The sample correlation coefficient for this area is 0.44, which is significant above the 99.9% level.

A potential problem with this interpretation though is that it corresponds to northwesterly back azimuths at CMAR. The data prefer southeasterly back azimuths (Fig. 4), corresponding to the southwestern quadrant of the seismic source annulus shown in Figure 7. Therefore, for this interpretation to be correct it must be the case that our slowness estimates are biased (on the order of 3–4 sec/deg) by imperfections in the slowness corrections of Bondar *et al.* (1999) or because of some deficiency in our observational techniques. For example, our slowness inference techniques assume a single plane wave model, and if multiple plane waves arrive in the same time window, it is possible that the peak of the dominant arrival is shifted somewhat in slowness space (e.g., Shumway *et al.*, 2008).

We next consider the possibility that the high-velocity noise peak observed at CMAR is created by energy that has reflected off the core–mantle boundary as *PcP* waves. This seems less plausible than the *PKP* hypothesis because *PcP* waves are relatively small, especially at small source–

receiver distances, and the corresponding direct *P* waves would be expected to be visible in the noise spectra with ray parameters of 6–9 sec/deg. Nevertheless, it is plausible that at least some of the high-velocity noise observed at CMAR is created in this manner.

In Figure 8 we show the correlation of the high-velocity noise time series with ocean wave heights for distances less than 90° from CMAR, which is equivalent to the hemisphere opposite that shown in Figure 7. The seemingly strong correlation in the Barents Sea is an artifact related to the extrapolation of our ocean height model to latitudes above what is covered by TOPEX/POSEIDON satellite tracks; however, the strong correlations observed across much of the north Pacific are legitimate. In the bottom panel we compare the seismic noise time series with wave heights from a domain just north of New Guinea, at a distance of around 50° from CMAR. A *PcP* wave from this area would arrive at CMAR with a ray parameter of 3.7 sec/deg from a back azimuth of around 100°. The sample correlation coefficient in this case is 0.37, which is significant above the 99.9% level. Equivalently strong positive correlations are found for regions in the North Pacific near the Aleutians, a region known for large wave heights.

A final possibility is that the high-velocity noise recorded at CMAR is created by direct teleseismic *P* waves that turn deep in the lower mantle. High correlation with ocean waves in the Pacific is seen for many regions at distances of 60°–90° from CMAR (Fig. 8). These *P* waves would arrive at CMAR from the east with ray parameters of 4.5–7.0 sec/deg, contradicting our observations by about 3–4 sec/deg in absolute slowness. But, this is the same margin of error as for the *PKP* interpretation and so for the rea-

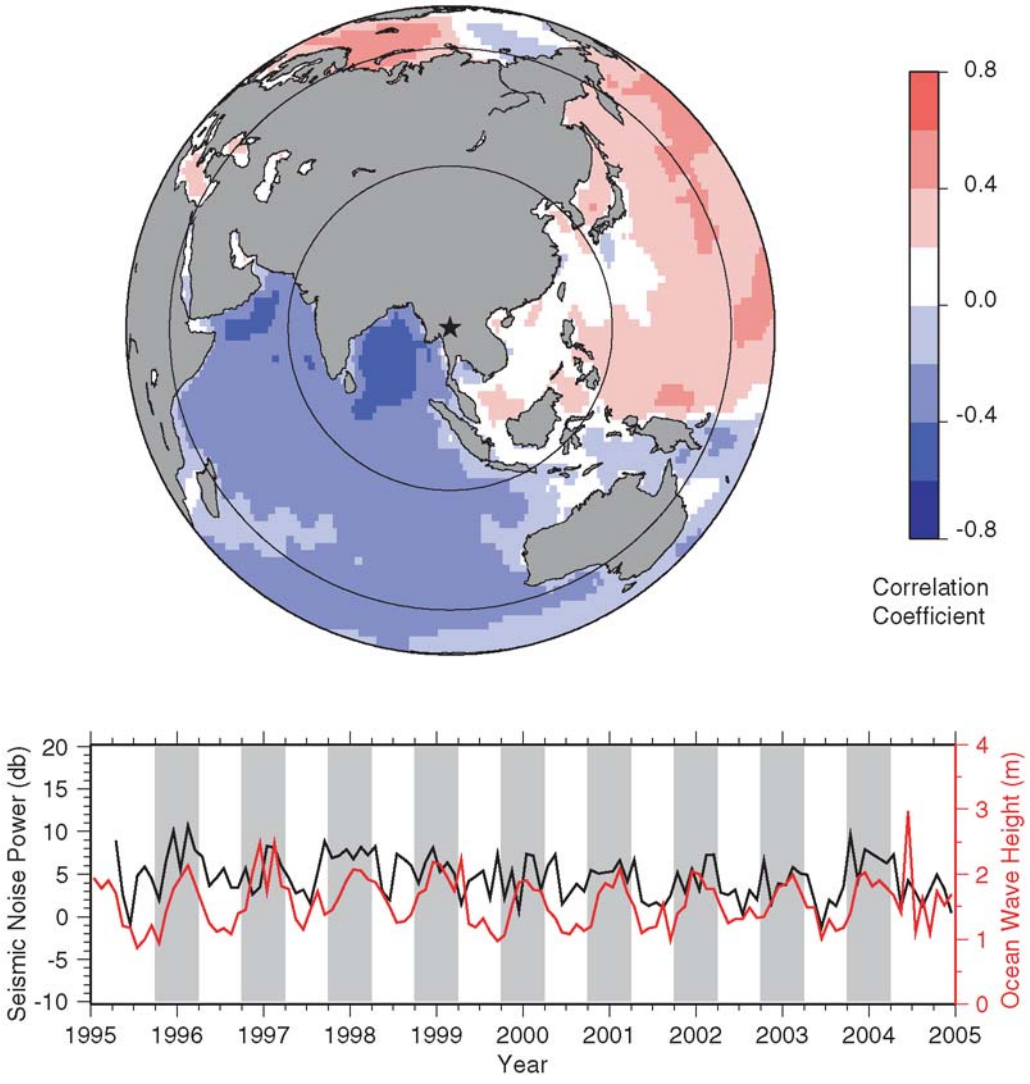

Figure 8. Correlation of the high-velocity microseismic energy with ocean wave heights, assuming a *P*/*PcP* source. In the top panel the circles are drawn at distances of 30° and 60° from CMAR, and the color indicates the correlation coefficient between the seismic noise and the significant ocean wave heights. The time dependence of the seismic noise is shown by the black curve in the bottom panel, and the red curve represents significant wave height for a domain just to the north coast of New Guinea defined as 0°–10° N and 135°–150° E.

sons mentioned earlier the teleseismic *P* energy could plausibly contribute to the observed noise.

Conclusions

We calculated *f-k* spectra for 955 samples of seismic noise recorded at the Chiang Mai seismic array (CMAR) from 1995 through 2004. At frequencies above about 1.4 Hz, the noise is isotropic and diffuse. Therefore, in array analysis of body waves from small regional events recorded at CMAR, the assumption of an isotropic noise model is justified and gains close to $\sqrt{18}$ are expected when processing high-passed waveforms with coherent signals.

At frequencies lower than 1.4 Hz, the noise at CMAR is strongly partitioned by apparent velocity into two categories: teleseismic *P*-wave energy with apparent velocities higher than 25 km/sec (with ray parameters of 0.0–5.0 sec/deg) and higher-mode Rayleigh energy with apparent velocities near 4.0 km/sec. The ring of slowness space in between, corresponding to *P* waves turning in the crust and upper mantle, is relatively quiet. The Rayleigh noise is further partitioned by direction, with the strongest signal arriving from the Bay of Bengal at back azimuths of 180°–255°. A secondary peak in the Rayleigh noise occurs in the direction of the South China Sea at back azimuths of 80°–120°. Little noise arrives from the north, the direction of the main Asian landmass and the nuclear test sites of India, Pakistan, China, and North Korea.

The Rayleigh noise is strongly seasonal with annual variations of 10–15 dB in power. The easterly noise has peaks in local winter and troughs in local summer, while the noise from the southwest has the opposite pattern. This behavior is well matched by the seasonal anticorrelation in significant wave heights in the South China Sea and the Bay of Bengal, as determined from TOPEX/POSEIDON satellite tracks. For a magnitude scale such as $M_S(V_{max})$ (Bonner *et al.*, 2006; Russell, 2006) that depends directly on the logarithm of seismic amplitude, our observations imply that the detection threshold at CMAR varies by 0.5–0.75 magnitude units according to direction and time of year.

While propagating Rayleigh waves are often observed in seismic noise, it is less common to observe teleseismic body waves. Nearly all reports of body-wave noise document ray parameters of 8–12 sec/deg, which correspond to *P* waves that turn in the upper mantle (e.g., Toksöz and Lacoss, 1968; Haubrich and McCamy, 1969; Cole *et al.*, 1989; Gerstoft *et al.*, 2006). Therefore, our observations of a consistent noise peak with ray parameters of 4.5 sec/deg and smaller, equivalent to apparent velocities of 25 km/sec and higher, may be unique in the geophysical literature.

Like the Rayleigh noise, the *P* noise observed at CMAR is seasonal. It has an annual power variation of 5–10 dB, with peaks in local winter and troughs in local summer. The seasonality implies that the noise is unrelated to small unidentified earthquakes or other tectonic processes and, instead, is created at least indirectly by ocean waves, similar to the Rayleigh noise. Under this assumption there are several geographical regions that could act as sources: the western Atlantic Ocean near the coast of northern Brazil may contribute *PKP* energy, the Pacific Ocean just north of New Guinea may contribute *PcP* energy, and central portions of the North Pacific may contribute *P* waves that turn in the lower mantle. However, none of these sources provides an ideal match to our slowness observations and so none are preferred over the others.

In order to resolve the uncertainty of the source location of the *P* noise at CMAR, a finer comparison of seismic data and ocean wave data is required. Ideally, we would compare daily or even hourly samples of seismic noise to the geographical tracks of named storms and/or to equally uniformly sampled ocean wave height data from buoys. Observations of *P* noise from other arrays in the general area would also help, especially if those arrays are slightly wider in aperture than CMAR with correspondingly smaller slowness biases related to near-receiver heterogeneity.

In any case, and irrespective of the precise source mechanism for the high-velocity noise, our observations point toward a new method of imaging the Earth's deep interior. Just as Rayleigh microseismic noise has been used to image the Earth's crust (Shapiro *et al.*, 2005), it may be possible to use microseismic *P* noise to image the Earth's lowermost mantle and core. This could be especially beneficial for regions of the deep Earth that are poorly sampled by present-day patterns of seismicity.

Data and Resources

The TOPEX/POSEIDON significant wave height data were obtained from the Physical Oceanography Distributed Active Archive Center (PO.DAAC) at the National Aeronautics and Space Administration (NASA) Jet Propulsion Laboratory (JPL), Pasadena, California. They are publically available. Seismograms used in this study were obtained from the U.S. National Data Center (NDC) maintained by the Air Force Technical Applications Center (AFTAC) in Melbourne, Florida. They are also available to the public.

Acknowledgments

The work presented here was funded by the U.S. Air Force Research Laboratory under Contract Number FA871806C0003. We are grateful to P.S. Callahan for assistance in working with the wave height data. We thank Anton Dainty, Fred Pollitz, and an anonymous referee for critical comments. We used the Generic Mapping Tool (GMT; Wessel and Smith, 1991) to make most of the figures.

References

Bokelmann, G. H. R. (1995). Azimuth and slowness deviation from the GERES regional array, *Bull. Seismol. Soc. Am.* **85,** 1456–1463.

Bondar, I., R. G. North, and G. Beall (1999). Teleseismic slowness-azimuth station corrections for the international monitoring system seismic network, *Bull. Seismol. Soc. Am.* **89,** 989–1003.

Bonner, J. L., D. R. Russell, D. G. Harkrider, D. T. Reiter, and R. B. Herrmann (2006). Development of a time-domain, variable-period surface-

wave magnitude measurement procedure for application at regional and teleseismic distances, part II: Application and M_s-m_b performance, *Bull. Seismol. Soc. Am.* **96,** 678–696.

Bungum, H., E. Rygg, and L. Bruland (1971). Short-period seismic noise structure at the Norwegian seismic array, *Bull. Seismol. Soc. Am.* **61,** 357–373.

Burg, J. (1964). Three-dimensional filtering with an array of seismometers, *Geophysics* **39,** 693–713.

Callahan, P. S., C. S. Morris, and S. V. Hsiao (1994). Comparison of TOPEX/POSEIDON σ_0 and significant wave height distributions to Geosat, *J. Geophys. Res.* **99,** 25,015–25,024.

Capon, J. (1969). High-resolution frequency-wavenumber spectrum analysis, *Proc. IEEE* **57,** 1408–1418.

Cessaro, R. K. (1994). Sources of primary and secondary microseisms, *Bull. Seismol. Soc. Am.* **84,** 142–148.

Cole, S., J. Claerbout, D. Nichols, and L. Zhang (1989). Ambient seismic field in three dimensions, in *59th Annual Internat. Mtg. Soc. Expl. Geophys.*, 395 pp.

Douglas, A. (1998). Making the most of the recordings from short-period seismometer arrays, *Bull. Seismol. Soc. Am.* **88,** 1155–1170.

Engdahl, E. R., and C. Felix (1971). Nature of travel time anomalies at LASA, *J. Geophys. Res.* **76,** 2706–2715.

Gerstoft, P., M. C. Fehler, and K. G. Sabra (2006). When Katrina hit California, *Geophys. Res. Lett.* **33,** L17308, doi 10.1029/2006GL027270.

Haubrich, R. A. (1968). Array design, *Bull. Seismol. Soc. Am.* **58,** 977–991.

Haubrich, R. A., and K. McCamy (1969). Microseismic: coastal and pelagic sources, *Rev. Geophys.* **7,** 539–571.

Ingate, S. F., E. S. Husebye, and A. Christoffersson (1985). Regional arrays and optimum data processing schemes, *Bull. Seismol. Soc. Am.* **75,** 1155–1177.

Koper, K. D., J. Franks, and M. Dombrovskaya (2004). Evidence for small-scale heterogeneity in Earth's inner core from a global study of PKiKP coda waves, *Earth Planet. Sci. Lett.* **228,** 227–241.

Lacoss, R. T., E. Kelly, and M. N. Toksöz (1969). Estimation of seismic noise structure using arrays, *Geophysics* **34,** 21–38.

Longuet-Higgins, M. (1950). A theory of the origin of microseisms, *Philos. Trans. R. Soc. Lond. A* **243,** 1–35.

Louie, J. (2001). Faster, better: shear-wave velocity to 100 meters depth from refraction microtremor arrays, *Bull. Seismol. Soc. Am.* **91,** 347–364.

Okada, H. (2003). *The Microtremor Survey Method*, Society of Exploration Geophysicists, Geophysical Monograph, **12**.

Rhie, J., and B. Romanowicz (2004). Excitation of Earth's continuous free oscillations by atmosphere-ocean-seafloor, *Nature* **431,** 552–556.

Rost, S., and T. Thomas (2002). Array seismology: methods and applications, *Rev. Geophys.* **40,** 1008, doi 10.1029/2000RG000100.

Russell, D. R. (2006). Development of a time-domain, variable-period surface-wave magnitude measurement procedure for application at regional and teleseismic distances, part I: Theory, *Bull. Seismol. Soc. Am.* **96,** 665–677.

Schimmel, M., and H. Paulssen (1997). Noise reduction and detection of weak, coherent signals through phase-weighted stacks, *Geophys. J. Int.* **130,** 497–505.

Schulte-Pelkum, V., P. S. Earle, and F. L. Vernon (2004). Strong directivity of ocean-generated seismic noise, *Geochem. Geophys. Geosys.* **5,** Q03004, doi 10.1029/2003GC000520.

Schweitzer, J., J. Fyen, S. Mykkeltveit, and T. Kvaerna (2002). Seismic arrays, in *IASPEI New Manual of Seismological Observatory Practice*, P. Bormann (Editor), GeoForschungsZentrum, Potsdam, chap. 9, 31–32.

Shapiro, N. M., M. Campillo, L. Stehly, and M. H. Ritzwoller (2005). High-resolution surface-wave tomography from ambient seismic noise, *Science* **307,** 1615–1618.

Shumway, R. H., E. Smart, and D. A. Clauter (2008). Mixed signal processing for regional and teleseismic arrays, *Bull. Seismol. Soc. Am.* **98,** 36–51.

Tibuleac, I., and E. Herrin (1997). Calibration studes at TXAR, *Seism. Res. Lett.* **68,** 353–365.

Toksöz, M. N., and R. T. Lacoss (1968). Microseism: mode structure and sources, *Science* **159,** 872–873.

Webb, S. C. (1998). Broadband seismology and noise under the ocean, *Rev. Geophys.* **36,** 105–142.

Wessel, P., and W. Smith (1991). Free software helps map and display data, *EOS Trans. AGU* **72,** 441, 445–446.

Department of Earth and Atmospheric Sciences
Saint Louis University
3642 Lindell Boulevard
St. Louis, Missouri 63108
koper@eas.slu.edu

Manuscript received 19 May 2008